

# Assignment 3

Sagar Poudel - 213051001  
Sejal Upadhye - 213050017

March 23, 2022

## 1 Q1

The original image is given as:



Figure 1: Original Barbara Image

### 1.1 (a)

RMSE due to noise: **0.0219**

RMSE after reconstruction: **0.0205**



Figure 2: Original image, image with noise, final reconstructed image

## 1.2 (b)

RMSE after reconstruction: **0.4043**

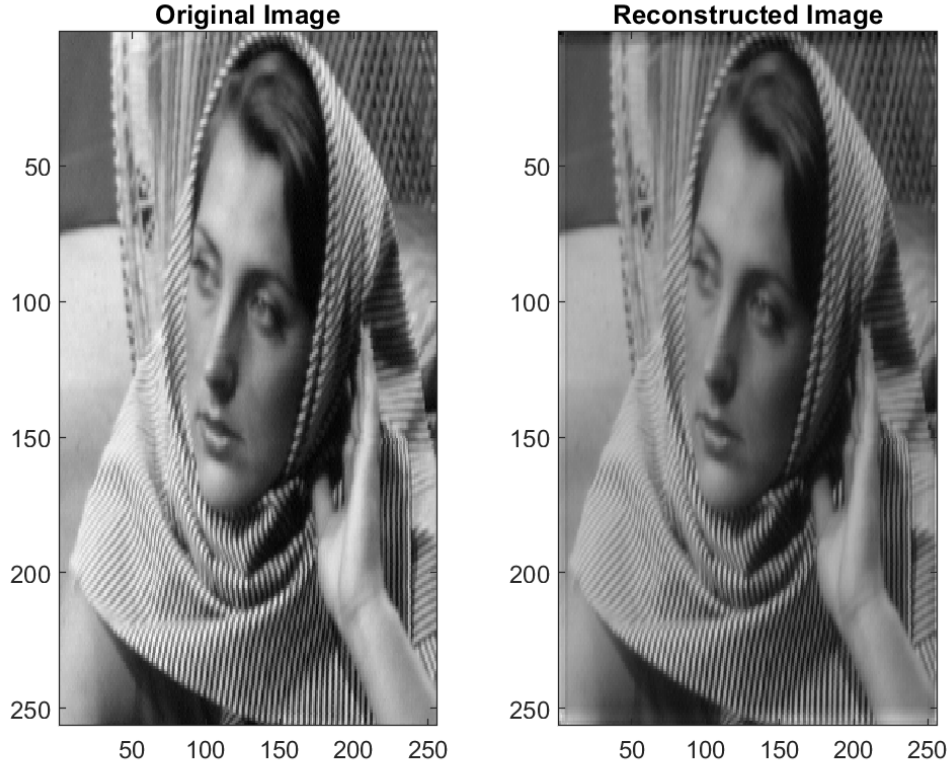


Figure 3: Original image, image with noise, final reconstructed image

## 2 Q2

### 2.1 (a)

The loss function is defined as:

$$f_N \beta = \frac{\|y - X\beta\|_2^2}{2N}$$

We want the above function to be strong convex. We would calculate the double derivative matrix  $\nabla^2 f(\beta) = X^T X / N$  and have condition that the eigenvalues of the  $p \times p$  be positive semi-definite matrix.  $X^T X$  has rank at most  $\min N, p$ , so it is always rank deficient.

We need to relax our notion of strong convexity and impose a type strong convexity condition on some subset  $C \subset \mathbf{R}^p$  of possible perturbation vector  $v \in \mathbf{R}^p$ . Thus, function  $f$  satisfies restricted strong convexity at  $\beta^*$  with respect to  $C$ .

$$\frac{v^T \nabla^2 f(\beta) v}{\|v\|_2^2} \geq \gamma \quad \forall \text{ non-zero } v \in C$$

This notion is equivalent to lower bounding the *restricted eigenvalues*

$$\frac{v^T X^T X v}{N \|v\|_2^2} \geq \gamma \quad \forall \text{ non-zero } v \in C$$

In this case, a bound on the function difference  $f_N = |f_N(\hat{\beta}) - f_N(\beta^*)|$  translates directly into a bound on  $\Delta\beta = \|\hat{\beta} - \beta^*\|_2$ .

## 2.2 (b)

It is given that  $\hat{\nu} := \hat{\beta} - \beta^*$  minimizes the equation:

$$G(\hat{\nu}) = \frac{\|\mathbf{y} - \mathbf{X}(\beta^* + \hat{\nu})\|_2^2}{2N} + \lambda_N \|(\beta^* + \hat{\nu})\|_1$$

Thus, as per the given fact above, we can write  $G(\hat{\nu}) \leq G(0)$

## 2.3 (c)

From the equation and fact given above we can write:

$$\frac{\|\mathbf{y} - \mathbf{X}(\beta^* + \hat{\nu})\|_2^2}{2N} + \lambda_N \|(\beta^* + \hat{\nu})\|_1 \leq \frac{\|\mathbf{y} - \mathbf{X}\beta^*\|_2^2}{2N} + \lambda_N \|\beta^*\|_1$$

Given  $y = X\beta^* + w$ , substituting value w.r.t. to w

$$\frac{\|w - \mathbf{X}\hat{\nu}\|_2^2}{2N} - \frac{\|w\|_2^2}{2N} \leq \lambda_N (\|\beta^*\|_1 - \|(\beta^* + \hat{\nu})\|_1)$$

Now, Expanding L2 Norm of  $\|w - \mathbf{X}\hat{\nu}\|_2^2$  and simplifying the equation we get,

$$-\frac{w^T \hat{\nu} \mathbf{X}}{N} + \frac{\hat{\nu}^T \mathbf{X}^T \mathbf{X} \hat{\nu}}{2N} \leq \lambda_N (\|\beta^*\|_1 - \|(\beta^* + \hat{\nu})\|_1)$$

Shifting the terms we get,

$$\frac{\|\mathbf{X}\hat{\nu}\|_2^2}{2N} \leq \frac{w^T \mathbf{X} \hat{\nu}}{N} + \lambda_N (\|\beta^*\|_1 - \|(\beta^* + \hat{\nu})\|_1)$$

## 2.4 (d)

Given,  $\beta_{S^c}^* = 0$ , and we have,  $\|\beta^*\|_1 = \|B_s^*\|_1$  and,

$$\|\beta^* + \hat{\nu}\|_1 = \|\beta_s^* + \hat{\nu}_s\|_1 + \|\hat{\nu}_{S^c}\|_1 \geq \|\beta_s^*\|_1 - \|\hat{\nu}_s\|_1 + \|\hat{\nu}_{S^c}\|_1$$

using this in previous equation from c, we get

$$\frac{\|\mathbf{X}\hat{\nu}\|_2^2}{2N} \leq \frac{w^T \mathbf{X} \hat{\nu}}{N} + \lambda_N (\|\hat{\nu}_s\|_1 - \|\hat{\nu}_{S^c}\|_1)$$

We know that,  $\frac{w^T \mathbf{X} \hat{\nu}}{N}$  is scalar and transpose is also same thus can be written as  $\frac{\hat{\nu}^T \mathbf{X}^T w}{N}$

Now finding product of these value:

$$\hat{\nu}^T \mathbf{X}^T w = \langle \hat{\nu}, \mathbf{X}^T w \rangle$$

Finding dot products as:

$$\langle \hat{\nu}, \mathbf{X}^T w \rangle = \sum_{i=1}^p \hat{\nu}_i (\mathbf{X}^T w)_i \leq \sum_{i=1}^p |\hat{\nu}_i| |(\mathbf{X}^T w)_i| \leq \max_i \{ |(\mathbf{X}^T w)_i| \} \sum_{i=1}^p |\hat{\nu}_i|$$

The above equation use Harold's inequality.

Now first term  $L_{\inf}$  term and second term is  $L_1$  term, we get

$$\langle \hat{\nu}, \mathbf{X}^T w \rangle = \|\mathbf{X}^T w\|_{\infty} \|\hat{\nu}\|_1$$

Substituting value in first equation of this question, we get:

$$\frac{\|\mathbf{X}\hat{\nu}\|_2^2}{2N} \leq \frac{\|\mathbf{X}^T w\|_{\infty}}{N} \|\hat{\nu}\|_1 + \lambda_N (\|\hat{\nu}_s\|_1 - \|\hat{\nu}_{S^c}\|_1)$$

## 2.5 (e)

Given,  $\frac{1}{N} \|\mathbf{X}^T w\|_\infty \leq \frac{\lambda_N}{2}$ , we have

$$\begin{aligned} \frac{\|\mathbf{X}\hat{\nu}\|_2^2}{2N} &\leq \frac{\lambda_N}{2} (\|\hat{\nu}_S\|_1 - \|\hat{\nu}_{S^c}\|_1) + \lambda_N (\|\hat{\nu}_S\|_1 + \|\hat{\nu}_{S^c}\|_1) \\ &= \frac{3}{2} \lambda_N \|\hat{\nu}_S\|_1 - \frac{1}{2} \lambda_N \|\hat{\nu}_{S^c}\|_1 \\ &\leq \frac{3}{2} \lambda_N \|\hat{\nu}_S\|_1 \\ &\leq \frac{3}{2} \sqrt{k} \lambda_N \|\hat{\nu}\|_2 \text{ (L1 to L2 conversion)} \end{aligned}$$

## 2.6 (f)

Using the restricted Eigenvalue condition from part (a), we have:

$$\frac{v^T \mathbf{X}^T \mathbf{X} v}{N \|v\|_2^2} \geq \gamma \quad \forall \text{ non-zero } v \in \mathbf{C}$$

Simplifying the equation we get:

$$\frac{\|\mathbf{X}\hat{\nu}\|_2^2}{2N} = \frac{v^T \mathbf{X}^T \mathbf{X} v}{2N} \geq \frac{\gamma \|\hat{\nu}\|_2^2}{2}$$

From equation in the previous part (e): we have

$$\frac{\gamma \|\hat{\nu}\|_2^2}{2} \leq \frac{\|\mathbf{X}\hat{\nu}\|_2^2}{2N} \leq \frac{3}{2} \sqrt{k} \lambda_N \|\hat{\nu}\|_2$$

Thus, final error bound is given as:

$$\|\hat{\beta} - \beta^*\|_2 = \|\hat{\nu}\|_2 \leq 3 \lambda_N \sqrt{k} N$$

## 2.7 (g)

This is an assumption taken for lemma 11.1 for the cone constraint that  $\|\hat{\nu}_{S^c}\|_1 \leq \|\hat{\nu}_S\|_1$ . We can use this assumption in part (e) to prove the cone constraint

$$\frac{\|\mathbf{X}\hat{\nu}\|_2^2}{2N} \leq \frac{3}{2} \lambda_N \|\hat{\nu}_S\|_1 - \frac{1}{2} \lambda_N \|\hat{\nu}_{S^c}\|_1$$

From the assumption we can set LHS to zero then, we get:

$$0 \leq \frac{3}{2} \lambda_N \|\hat{\nu}_S\|_1 - \frac{1}{2} \lambda_N \|\hat{\nu}_{S^c}\|_1$$

Thus,

$$\|\hat{\nu}_{S^c}\|_1 \leq 3 \|\hat{\nu}_S\|_1$$

## 2.8 (h)

In the beginning, we saw that convex loss function of high dimensional setting may not be strongly convex. To ease the notion of strong convexity, we only impose strong convexity in some subset  $C \in \mathbf{R}^p$ . Defining lasso error  $\hat{\nu} = \hat{\beta} - \beta^*$ , with proper choice or equivalently, of regularization constant, it leads to a cone constraint of the form  $\|\hat{\nu}_{S^c}\|_1 \leq 3 \|\hat{\nu}_S\|_1$

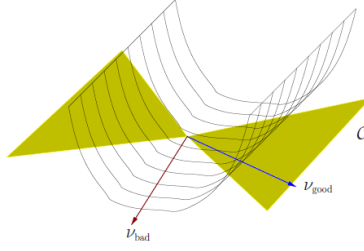


Figure 4: A convex loss function in high-dimensional settings (with  $p \gg N$ ) cannot be strongly convex; rather, it will be curved in some directions but flat in others

## 2.9 (i)

In this theorem, with known support set,  $l_2$  error decays more quickly than  $\frac{k}{N}$ , where,  $k$  is the sparsity and  $N$  is the number of the measurement  $x$  compare to any other methods like theorem 3. Apart from the logarithmic factor, the lasso rate matches the best possible one can achieve, i.e. it is known to be minimax optimal, meaning that it cannot be substantially improved upon by any estimator.

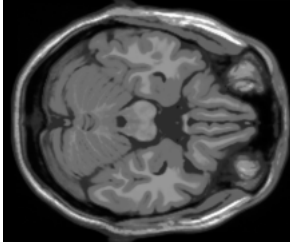
One advantage of theorem 3 over this theorem is that, error observed using oracle error gives more detail about the reconstruction error compared to this theorem.

## 2.10 (j)

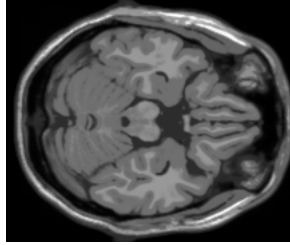
The common thread between the bounds on the ‘Dantzig selector’ and the LASSO is that both provides similar guarantees for  $l_1$  minimization where Dantzig selector sets  $\|A^T e\|_\infty \leq \lambda$ . Similar type of results were achieved in Dantzig selector, where error bounds by a constant times  $k\sigma^2 \log n$  with high probability.

## 3 Q3

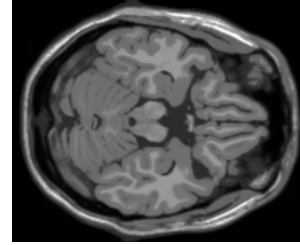
For this question, we have considered following three images and have padded to 225 for the ease of calculation:



Slice 50



Slice 51



Slice 52

Figure 5: Original Images

## 3.1 (a)

Filtered Back Projection using **Ram-Lak** Filter reconstruction result for slice 50 and 51 using 18 uniformly spaced angle for measurement is given below:

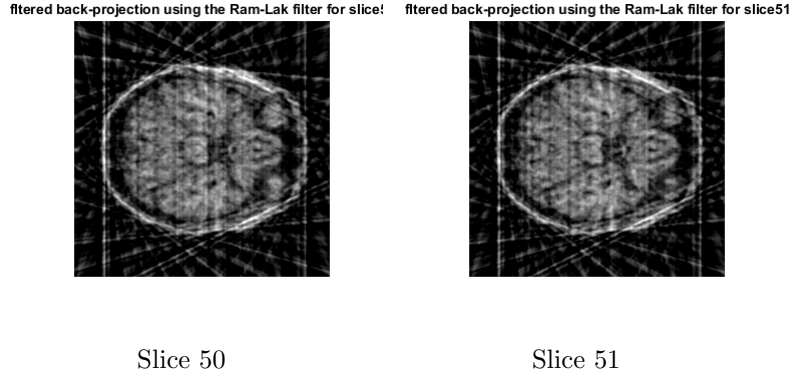


Figure 6: Reconstruction using 18 uniformly spaced angle for measurement

### 3.2 (b)

Referring from Tomography slides 41, the Tomographic reconstruction using **Independent Compressed Sensing** for each slices by solving following loss function:

$$E(\beta) = ||y - RU\beta||^2 + \lambda||\beta||_1$$

The reconstruction is given as:

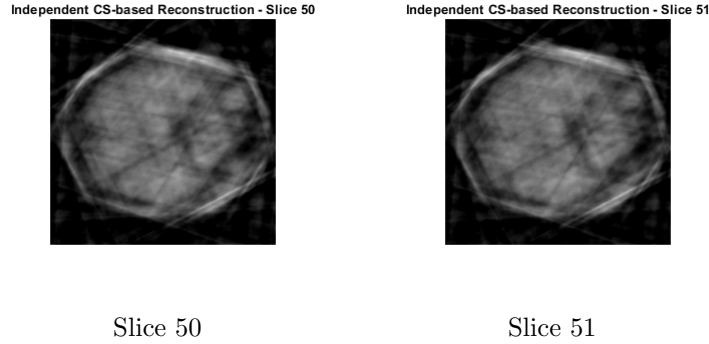


Figure 7: Reconstruction using 18 uniformly spaced angle for measurement using independent compressed sensing reconstruction

### 3.3 (c)

Referring from Tomography slides 49, the Tomographic reconstruction using **Coupled Compressed Sensing** for each slices by solving following loss function:

$$E\left(\begin{bmatrix} \beta_1 \\ \Delta\beta_1 \end{bmatrix}\right) = \left\| \begin{bmatrix} y_1 \\ y_2 \end{bmatrix} - \begin{bmatrix} R_1U & 0 \\ R_2U & R_2U \end{bmatrix} \begin{bmatrix} \beta_1 \\ \Delta\beta_1 \end{bmatrix} \right\|_2^2 + \lambda \left\| \begin{bmatrix} \beta_1 \\ \Delta\beta_1 \end{bmatrix} \right\|_1$$

Here,

- $y_1$  and  $y_2$  represent their tomographic projections expressed as 1D vectors.
- $\beta_1$  is the 2D-DCT of first slice  $x_1$  as 1D vectors
- $\beta_1 + \Delta\beta_1$  is the 2D-DCT of second slice as 1D vectors
- $R_1$  and  $R_2$  are the radon transform matrix for random angles to compute the tomographic projection of  $x_1$  and  $x_2$  respectively.

The reconstruction of two slices 50 and 51 is given as:

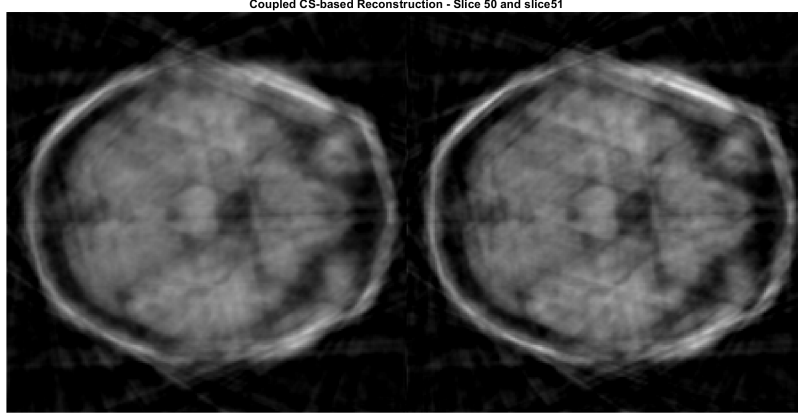


Figure 8: Left:Slice 50, right: Slice 51, Reconstruction using 18 uniformly spaced angle for measurement using coupled compressed sensing reconstruction(2 slices)

### 3.4 (d) - Using 3 slices for coupled sensing

Referring from Tomography slides 49, the Tomographic reconstruction using **Coupled Compressed Sensing** for each slices by solving following loss function:

$$E\left(\begin{bmatrix} \beta_1 \\ \Delta\beta_1 \\ \Delta\beta_2 \end{bmatrix}\right) = \left\| \begin{bmatrix} y_1 \\ y_2 \\ y_3 \end{bmatrix} - \begin{bmatrix} R_1U & 0 & 0 \\ R_2U & R_2U & 0 \\ R_3U & 0 & R_3U \end{bmatrix} \begin{bmatrix} \beta_1 \\ \Delta\beta_1 \\ \Delta\beta_2 \end{bmatrix} \right\|_2^2 + \left\| \begin{bmatrix} \beta_1 \\ \Delta\beta_1 \\ \Delta\beta_2 \end{bmatrix} \right\|_1$$

where,

- $y_1$  and  $y_2$  represent their tomographic projections expressed as 1D vectors.
- $\beta_1$  is the 2D-DCT of first slice  $x_1$  as 1D vectors
- $\beta_1 + \Delta\beta_1$  is the 2D-DCT of second slice  $x_2$  as 1D vectors
- $\beta_1 + \Delta\beta_2$  is the 2D-DCT of third slice  $x_3$  as 1D vectors
- $R_1, R_2$  and  $R_3$  are the radon transform matrix for random angles to compute the tomographic projection of  $x_1, x_2$  and  $x_3$  respectively.
- $U$  is 2D-DCT basis matrix

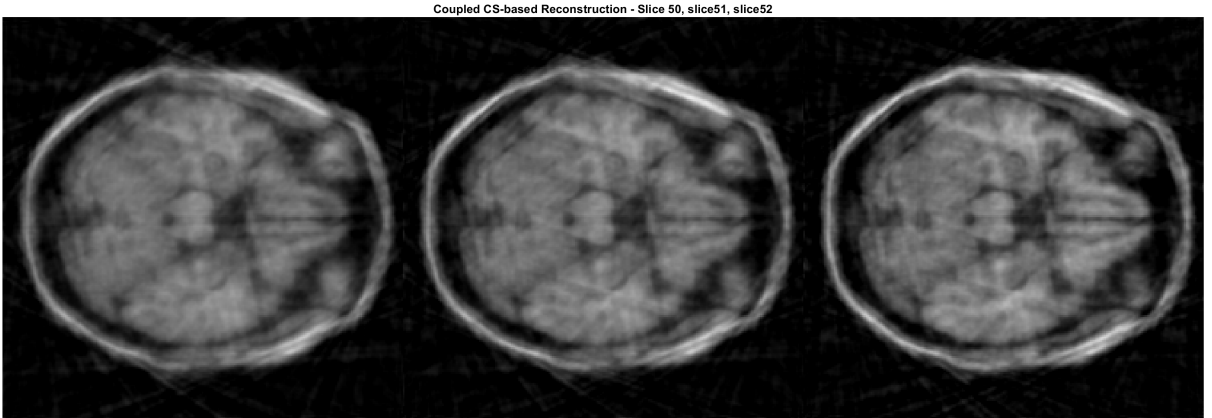


Figure 9: Left:Slice 50, middle: Slice 51, right: Slice 52 Reconstruction using 18 uniformly spaced angle for measurement using coupled compressed sensing reconstruction(3-slices)

## 4 Q4

**Title** - Inline discrete tomography system: Application to agricultural product inspection

**Author** - Luis F. Alves Pereira, Eline Janssens, George D.C. Cavalcanti, Tsang Ing Ren, Mattias Van Dael, Pieter Verboven, Bart Nicolai, Jan Sijbers.

**Year of Publication** - 2017

X-ray Computed Tomography (CT) has been applied in agriculture engineering for quality and defect control in food products. However, conventional CT systems are neither cost effective nor flexible, making the deployment of such technology unfeasible for many industrial environments. In this work, the authors propose a simple and cost effective X-ray imaging setup that comprises a linear translation of the object in a conveyor belt with a fixed X-ray source and detector, with which a small number of X-ray projections can be acquired within a limited angular range. Due to the limitations of such geometry, conventional reconstruction techniques lead to misshapen images. Therefore, a Discrete Tomography reconstruction technique is applied that incorporates prior knowledge of the density of the object's materials. Moreover, there is further improvement in the reconstruction results with the following strategies: (i) an image acquisition involving object rotation during a linear translation in the conveyor-belt; and (ii) an image reconstruction incorporating prior knowledge of the object support (e.g., obtained from optic sensors). Experiments based on simulation as well as real data demonstrate substantial improvement of the reconstruction quality compared to conventional reconstruction methods.

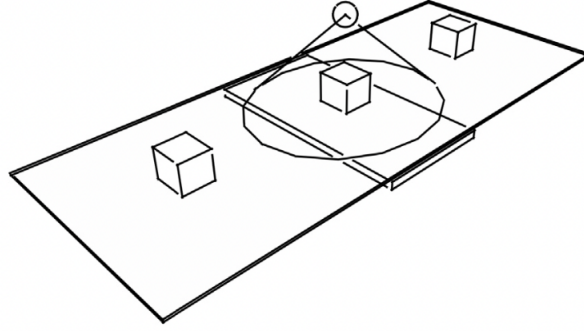


**Fig. 1.** Overview of the proposed inline scanning geometry: a wide cone X-ray source and a large detector are fixed for imaging objects passing on a conveyor belt.

Algebraic Reconstruction Methods (ARM) cast the reconstruction problem into a system of linear equations, which can be applied to different scanning geometries, and they can easily be augmented with object's prior knowledge to compensate a lack of scanned data. If  $\mathbf{v} \in \mathbb{R}^N$  is the vector associated with the reconstructed image, and the vector  $\mathbf{p} \in \mathbb{R}^M$  denotes the projection data of the scanned object, one can write:

$$\mathbf{p} = \mathbf{W}\mathbf{v} \quad (1)$$

where  $\mathbf{W}_{M \times N}$  is the projection matrix, which maps the vector representing the image in the reconstruction domain into the projection domain. Each element  $w_{m,n}$  in  $\mathbf{W}$  defines the contribution of voxel  $n$  in  $\mathbf{v}$  to the detector cell  $m$  in  $\mathbf{p}$ . An estimate of  $\mathbf{v}$  can then be found by minimizing the following function

$$\chi^2 = |\mathbf{W}\mathbf{v} - \mathbf{p}|^2 \quad (2)$$

- **Simultaneous Iterative Reconstruction Technique (SIRT)** An approximated solution to the least squares problem presented in (2) can be found by applying SIRT. It is a reconstruction technique that iteratively updates partial solutions  $\mathbf{v}^{(k)}$  where  $k$  denotes the iteration number. Assuming the typical initialization  $\mathbf{v}^{(0)} = 0$ , each SIRT iteration consists of three steps:



1. Compute the forward projection of the current solution:

$$\mathbf{p}^{(k)} = \mathbf{W}\mathbf{v}^{(k)} \quad (3)$$

2. Compute the *residual sinogram*:

$$\mathbf{r}^{(k)} = \mathbf{p} - \mathbf{p}^{(k)} \quad (4)$$

3. Update the reconstruction image  $\mathbf{v}^{(k)}$  by adding a weighted backprojection of the *residual sinogram* to the current solution:

$$\mathbf{v}^{(k+1)} = \mathbf{v}^{(k)} + \mathbf{C}\mathbf{W}^T\mathbf{R}\mathbf{r}^{(k)} \quad (5)$$

where  $\mathbf{R} \in \mathbb{R}^{m \times m}$  is a diagonal matrix with elements  $r_{ii} = 1/\sum_j w_{ij}$ .

Likewise,  $\mathbf{C} \in \mathbb{R}^{n \times n}$  is a diagonal matrix with elements  $c_{jj} = 1/\sum_i w_{ij}$ . The SIRT reconstruction process ends when a given convergence criterion is met.

- **Discrete Algebraic Reconstruction Technique (DART)** If there are only few X-ray projections  $\mathbf{p} \in \mathbb{R}^M$  available to reconstruct the image  $\mathbf{v} \in \mathbb{R}^N$ , i.e.  $M \ll N$ , the solution space of the minimization problem (2) is infinitely large. The idea behind using prior knowledge in the reconstruction process is to reduce the solution space by constraining the set of possible solutions. DART, for instance, assumes that the reconstruction is composed of only a few different materials which are represented by a small number of gray values in  $\mathbf{v} \in \mathbb{R}^N$ . Since in many food examples its inner composition can be well represented by only a small number of gray levels, DART was applied in this work. The DART workflow is based on the interleaving of continuous update steps and gray level discretization steps, which constrain the grey levels of the current solution to the expected densities of the scanned materials  $(\rho_1, \rho_2, \dots, \rho_l)$  which are seen as gray values in the reconstructed image. The flow chart shown in Fig. 2 describes the steps within DART. One DART iteration is composed of the following steps:

- Compute an initial ARM reconstruction
- Segment the reconstruction
- Identify non-fixed pixels U
- Identify fixed pixels F
- Apply new ARM iterations to the pixels in U while keeping the pixels in F fixed
- Stop criterion met
- Smooth the reconstruction

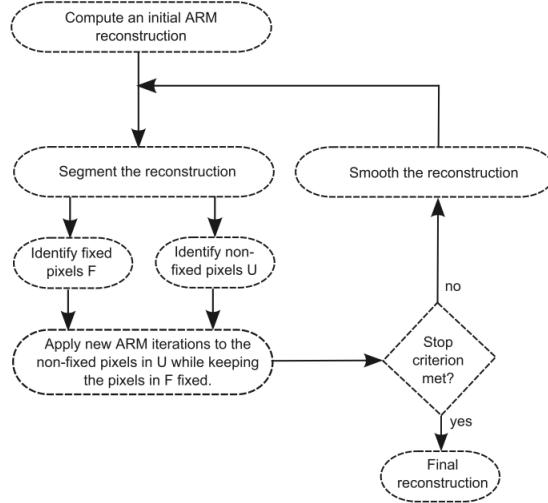


**Fig. 2.** Flow chart of DART: an initial ARM reconstruction is computed; then, a segmentation is applied; next, the image pixels are divided into fixed pixels and non-fixed pixels; next, new ARM iterations are applied only to the non-fixed pixels; finally, if the stop criterion is met, the algorithm ends, otherwise the solution is smoothed and the overall process restarts.

The proposed setup comprises a fixed cone beam X-ray source, a large detector, and a conveyor belt. In such scheme, the objects are imaged while they pass on a conveyor belt. The geometry of this setup is outlined in Fig. 3. The measures  $D$ ,  $B$ ,  $2a$ ,  $2L$ , and  $2\alpha$  are defined as Distance from the object to the X-ray source, Distance from the object to the detector, Length of the square which circumscribe the object, Detector length, and Fanbeam opening angle of the X-ray source. Such scanning setup differs from a conventional circular geometry in the following ways:

- **Limited angular range:** conventional X-ray sources available nowadays have cone angles limited to 60 degrees. In the inline geometry, where the radiation source is fixed, the available area for object sampling is restricted by the conebeam angular range.
- **Limited number of projections:** to reduce both the acquisition time and the reconstruction time, and also allow a higher translation velocity of the object in the conveyor belt, only a few number of projections should be acquired.

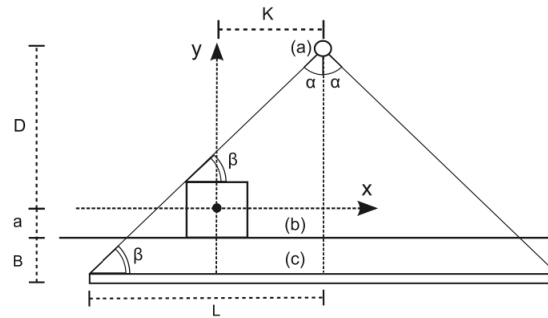


**Fig. 3.** Reference frame of the evaluated inline scanning geometry. The whole system is composed by a wide cone X-ray source (a), a conveyor belt (b) and a large detector (c).

- **Truncated projections:** projection data is lost near the detector borders. In fact, the object is only completely entailed by the X-ray fanbeam when the distance between the object and the X-ray source is no larger than  $K_m a x$ . From Fig. 3, the value of  $K_m a x$  can be calculated as follows:

$$\tan \beta = \frac{D - a}{K_{max} + a} = \frac{D + B + a}{L}$$

$$K_{max} = \frac{(D - a)}{(D + B + a)} \cdot L - a$$

The approaches proposed in this work to improve the image reconstruction quality in the proposed inline scanning geometry are as follows : The first approach involves the object rotation around its own axis in the conveyor belt to allow a full angular sampling; the second approach involves optical sensors to capture the outer object shape during a scanning process and include this information in a domain constrained reconstruction.

- **Scanning geometry with object rotation** A variation of the proposed setup is evaluated at which the object rotates around its own axis while it is linearly translated on a conveyor belt. Fig. 4(a) illustrates such rotation for subsequent time points. The proposed rotation allows a higher angular sampling about the scanned object. This way, the effects of the **limited angular range** in the proposed inline scanning setup is reduced. Fig. 4(b) shows examples of gears that can be used to allow the proposed movement of objects in the conveyor belt: a non-fixed pinion gear attached to a fixed rack gear; as the pinion gear rolls over the rack gear, both rotation and translation are obtained.

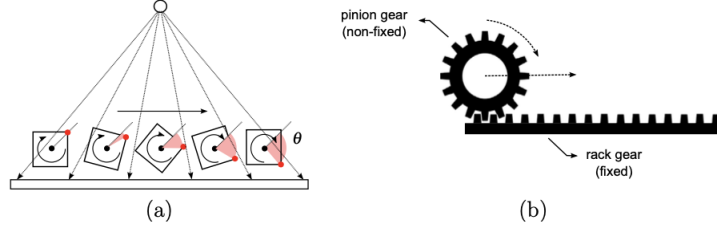


**Fig. 4.** The proposed object rotation of  $\theta$  in the conveyor belt during a linear translation (a); and the devices suggested to promote both rotation and translation of the object in the conveyor belt (b): a non-fixed pinion gear is attached to a fixed rack gear, the desired movement is produced as the pinion gear rolls over the rack gear.

- **Domain constrained discrete tomography** If the outer object shape is known in advance, the background pixels can be removed from the reconstruction domain. This way, the **limited number of projections** available in the proposed setup are used to calculate only a subset of the whole set of unknown pixels. In order to determine an object contour, optical sensor systems can be incorporated in the inline scanning geometry. In this work, an extension of DART which exploits the Expected Object Domain (EOD) referred to as EOD-DART is developed and evaluated. EOD-DART exploits prior knowledge of the object support (e.g., extracted from optical sensors) by restricting the ARM iterations to the pixels within the expected object domain, as illustrated in the flow chart of Fig. 5. In practice, the EOD can for example be obtained by segmenting an image captured by optical sensors. A simple segmentation technique like thresholding is usually sufficient to create an EOD **pixels U** from the segmented reconstruction. The pixels selected to be updated (i.e., which composes the **set of non-fixed pixels U**) are evaluated in respect to their position in the EOD matrix: the pixels which lie outside the EOD are allocated to the **set of fixed pixels F**. As a result, only pixels that lie inside the EOD can be candidate for update. After applying new ARM iterations to the pixels within the **set of non-fixed pixels U**, a partial EOD-DART result is obtained. If the stop criterion is met, the execution ends. Otherwise, a new iteration is computed as illustrated in Fig. 2.

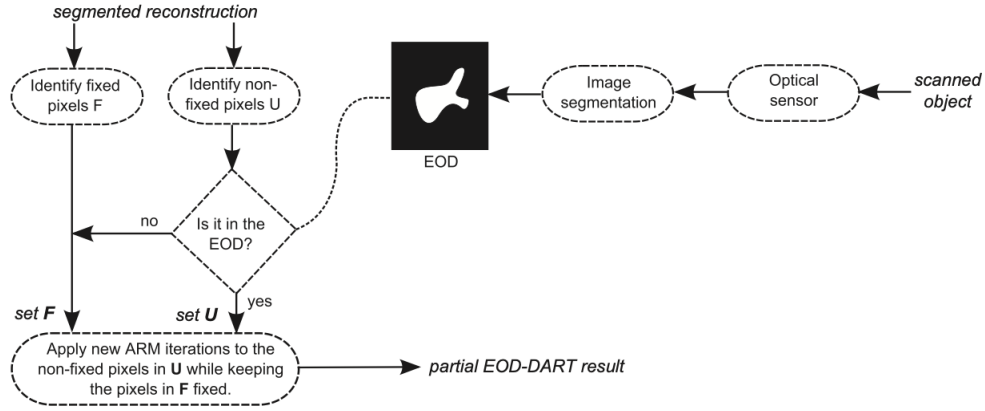


**Fig. 5.** Variation in flow chart proposed for EOD-DART in relation to DART: the pixels outer the object's domain are removed from the **set of non-fixed pixels U** at each DART iteration.

The following are the results obtained :

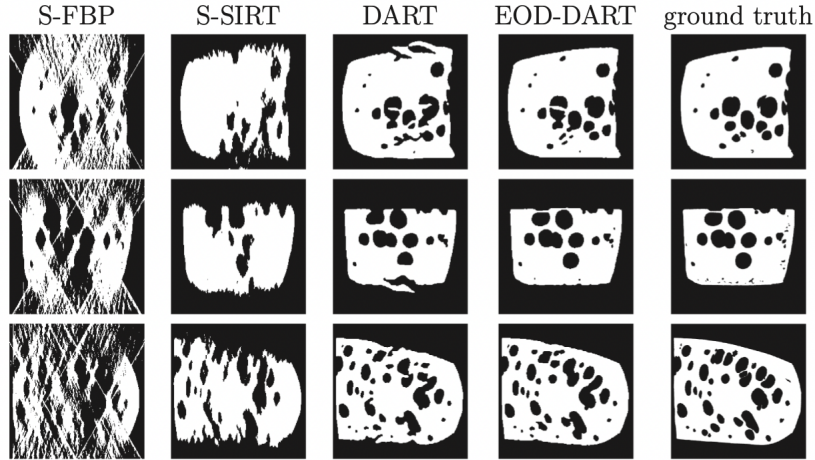


**Fig. 8.** Reconstructions of simulated cross-sections of cheese in the regular conveyor belt using 17 projections and X-ray opening angle  $2\alpha = 60^\circ$ . Each column presents solutions of distinct reconstruction algorithms: S-FBP, S-SIRT, DART, and EOD-DART, respectively. The last column shows the ground truth images.

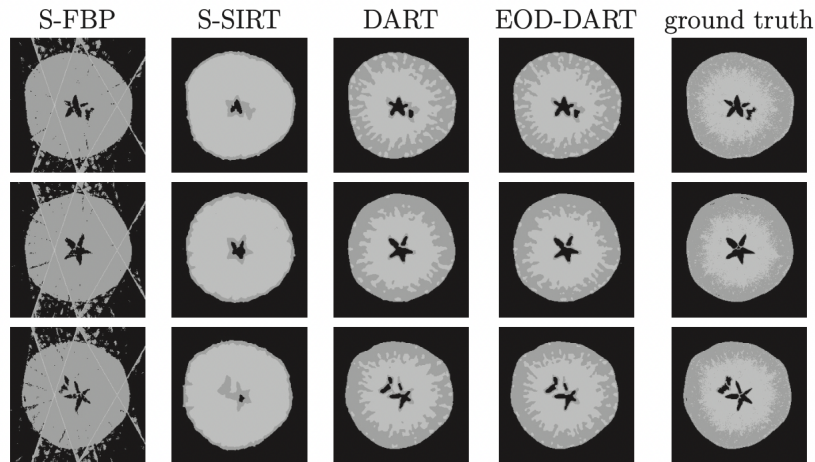


**Fig. 11.** Reconstructions of real cross-sections of apple in the conveyor belt with object rotation ( $\theta = 180^\circ$ ) using 17 projections and X-ray opening angle  $2\alpha = 60^\circ$ . Each column presents solutions of distinct reconstruction algorithms: S-FBP, S-SIRT, DART and EOD-DART, respectively. The last column shows the ground truth images.

## 5 Q5

The radon transform of the image  $f(x, y)$  is given as:

$$R_\theta(f) = R(f(x, y))(\rho, \theta) = \int_{-\infty}^{\infty} \int_{-\infty}^{\infty} f(x, y) \delta(x \cos \theta + y \sin \theta - \rho) dx dy$$

The radon transform of the scaled image  $f(ax, ay)$  where  $a \neq 0$  is given as

$$R(f(ax, ay))(\rho, \theta) = \int_{-\infty}^{\infty} \int_{-\infty}^{\infty} f(ax, ay) \delta(x \cos \theta + y \sin \theta - \rho) dx dy$$

Now, let consider  $u = ax, y = ay$

$$\begin{aligned} R'(f(u, v))(\rho, \theta) &= \frac{1}{a^2} \int_{-\infty}^{\infty} \int_{-\infty}^{\infty} f(ax, ay) \delta\left(\frac{u}{a} \cos \theta + \frac{v}{a} \sin \theta - \rho\right) dx dy \\ &= \frac{1}{a^2} \int_{-\infty}^{\infty} \int_{-\infty}^{\infty} f(u, v) \delta(a(u \cos \theta + v \sin \theta - \rho/a)) dx dy \\ &= \frac{1}{a} \int_{-\infty}^{\infty} \int_{-\infty}^{\infty} f(u, v) \delta(u \cos \theta + v \sin \theta - \rho/a) dx dy \\ &= \frac{1}{a} R(f(u, v))(\rho/a, \theta) \\ &= \frac{1}{a} R_\theta(f(x, y))(\rho/a, \theta) \end{aligned}$$

Therefore,

$$R_\theta(f(ax, ay))(\rho, \theta) = \frac{1}{a} R_\theta(f(x, y))(\rho/a, \theta)$$

## 6 Q6

The unit impulse function or Dirac Delta  $\delta(x, y)$  is given as:

$$\delta(x, y) = \begin{cases} 0, & \text{if } x \neq 0 \text{ and } y \neq 0 \\ 1, & \text{if } x = 0 \text{ and } y = 0 \end{cases}$$

The integration of Dirac Delta function is given as:

$$\int_{-\infty}^{\infty} \int_{-\infty}^{\infty} \delta(x, y) dx dy = 1$$

Since,

$$\int_{-\infty}^{\infty} \int_{-\infty}^{\infty} \delta(x, y) dx dy = \begin{cases} 0, & \text{if } x \neq 0 \text{ and } y \neq 0 \\ 1, & \text{if } x = 0 \text{ and } y = 0 \end{cases}$$

Therefore with dirac delta function, the radon transform is given as

$$R_\theta(f) = \int_{-\infty}^{\infty} \int_{-\infty}^{\infty} f(x, y) \delta(x \cos \theta + y \sin \theta - \rho) dx dy = \int_{-\infty}^{\infty} \int_{-\infty}^{\infty} f(0, 0) \delta(0, 0) dx dy = \begin{cases} f(0, 0), & \rho = 0 \\ 0, & \rho \neq 0 \end{cases}$$

Now, for the shifted unit impulse  $\delta(x-x_0, y-y_0)$ , here, we need to satisfy the condition  $x-x_0=0/y-y_0=0$  so that we get 1 after integration, thus  $x=x_0$  and  $y=y_0$

Thus,

$$\int_{-\infty}^{\infty} \int_{-\infty}^{\infty} f(x, y) \delta((x-x_0) \cos \theta + (y-y_0) \sin \theta - \rho) dx, dy = \begin{cases} f(x_0, y_0), & \rho = x_0 \cos \theta + y_0 \sin \theta \\ 0, & else \end{cases}$$